Journal of Materials Chemistry A

RSC Publishing

PAPER

View Article Online
View Journal | View Issue

Cite this: J. Mater. Chem. A, 2013, 1, 13301

Nanosized MnO_2 spines on Au stems for high-performance flexible supercapacitor electrodes†

Yu-Liang Chen,[a] Po-Chin Chen,[a] Tze-Lung Chen,[a] Chi-Young Lee[b] and Hsin-Tien Chiu*[a]

Received 26th July 2013
Accepted 3rd September 2013

DOI: 10.1039/c3ta12911j

www.rsc.org/MaterialsA

Electrodes composed of ultrathin MnO_2 (thickness 5–80 nm) spines on Au nanowire (NW) stems (length 10–20 μm, diameter 20–100 nm) were electrochemically grown on flexible polyethylene terephthalate (PET) substrates. The electrodes demonstrated high specific capacitance, high specific energy value, high specific power value, and long-term stability. In Na_2SO_4(aq.) (1 M), the maximum specific capacitance was determined to be 1130 F g^{-1} by cyclic voltammetry (CV, scan rate 2 mV s^{-1}) using a three-electrode system. From a galvanostatic (GV) charge/discharge test using a two-electrode system, a maximum capacitance of 225 F g^{-1} (current density 1 A g^{-1}) was measured. Even at a high charge/discharge rate of 50 A g^{-1}, the specific capacitance remained at an extremely high value of 165 F g^{-1}. The flexible electrodes also exhibited a maximum specific energy of 15 W h kg^{-1} and a specific power of 20 kW kg^{-1} at 50 A g^{-1}. After five thousand cycles at 10 A g^{-1}, 90% of the original capacitance was retained. A highly flexible solid-state device was also fabricated to reveal its supercapacitance performance.

Introduction

Due to the demand for many applications, development of effective energy storage devices, such as batteries and supercapacitors, has been extensively carried out.[1–4] Supercapacitors are promising because of their high specific power, fast charging/discharging rate, sustainable cycling life, and excellent cycle stability.[2,5] Large specific capacitances of electrochemical supercapacitors are the results of two mechanisms occurring at or near their electrode–electrolyte interfaces. The first one, based on charge separation at the interface, offers the double-layer capacitance through a non-Faradic process. The second one, dependent on redox reaction of the electrode materials, provides the pseudocapacitance *via* a Faradic process.[2,5] Many electrode materials, including a variety of carbon materials, various transition metal oxides (RuO_2, MnO_2, Co_3O_4, NiO, VO_x, and TiO_2), and several conducting polymers (polyaniline, polypyrrole, and polythiophene), have been widely researched for supercapacitor applications.[6–23] Among them, transition metal oxides are considered as the best candidates for redox supercapacitors because they possess a range of oxidation states.[24,25] In these metal oxides, MnO_2 is highly promising because of its high theoretical specific capacitance of 1370 F g^{-1}, high natural abundance, low cost, and low toxicity.[26] However, its low electrical conductivity of 10^{-5} to 10^{-6} S cm^{-1} presents a major challenge.[27] To overcome this problem, several strategies employing MnO_2-based nanostructures have been developed recently. In the first one, thin films or nanosized structures were fabricated to increase the surface areas for effective electrolyte contacts.[28,29] However, the poor electrical conductivity issue still existed. In another strategy, MnO_2 particles were coated onto conductive materials, such as metal, carbon materials, and conducting polymers, to enhance the supercapacitor performances.[30–40] However, when a large amount of MnO_2 was loaded onto an electrode, the oxide's high thickness not only limited the surface area/mass ratio but also restricted the electrolyte from participating in the electrochemical charge storage process. These increased the contact resistance and decreased the specific capacitance significantly. To overcome the drawbacks described above, coating thin layers of MnO_2 on high surface area conductive nanowires (NWs) composed of carbon-based and oxide-based composites has been intensively investigated.[41–45] In principle, they provide large interfacial areas for electrochemical reactions, short ion diffusion pathways, high electron transport rates, and increased charge/discharge performance. However, their multi-step fabrications are relatively complex. On the other hand, investigations on the deposition of MnO_2 on simple metal NWs are few. In a rare case, MnO_2 was fabricated on lithographically patterned Au NWs.[46] Although the structure is simple, the fabrication is still complicated. In this work, we will report simple electrochemical depositions of high density nanosized MnO_2 spines on Au stems (NMSAS) directly on flexible

[a]Department of Applied Chemistry, National Chiao Tung University, Hsinchu, Taiwan 30010, Republic of China. E-mail: htchiu@nctu.edu.tw

[b]Department of Materials Science and Engineering, National Tsing Hua University, Hsinchu, Taiwan 30013, Republic of China

† Electronic supplementary information (ESI) available. See DOI: 10.1039/c3ta12911j

polyethylene terephthalate (PET) substrates. In addition, we will discuss their much improved electrochemical properties for potential supercapacitor applications.

Experimental section

Chemicals and instruments

$HAuCl_4 \cdot 3H_2O$ (99%) and polyvinyl alcohol (PVA, M_w 85 000–124 000) were purchased from Sigma-Aldrich. Cetyl trimethylammonium chloride (CTAC, 890 mM) was supplied by Taiwan Surfactant. $NaNO_3$ was purchased from Riedel-de Haën. $Mn(NO_3)_2 \cdot 3H_2O$ (98%) was supplied by Alfa Aesar. Na_2SO_4 (99.3%) was purchased from Macron Chemicals. H_3PO_4 (85%) was purchased from J. T. Baker. Aqueous solutions were prepared in deionized water (DI water, MilliQ, 18 MΩ). The separators (membrane filters, grade: C020A047A, pore size: 2 μm) were purchased from Advantec. All experiments were performed at room temperature.

Scanning electron microscopy (SEM) images and energy dispersive spectroscopy (EDS) data were obtained using a JEOL JSM-7401F (15 keV). Transmission electron microscopy (TEM) images and selected-area electron diffraction (SAED) patterns were taken using a JEOL JEM-3000F (300 kV). X-ray photoelectron spectroscopy (XPS) data were collected using a ULVAC-PHI PHI Quantera SXM/Auger. Thin films were grown by using an e-gun evaporation system AST PEVA 600I. Electrochemical deposition experiments were performed with a direct current (DC) power supply GW Instek GPS-1830D. Cyclic voltammetry (CV), galvanostatic (GV) constant-current charge/discharge, and electrochemical impedance spectroscopic (EIS) measurements were performed using a CHI 6081C electrochemical workstation.

Fabrication of Au nanowires (NWs) on a flexible substrate

Thin layers of Ti (20 nm) and Au (80 nm) were evaporated sequentially onto a polyethylene terephthalate (PET) transparency to form a flexible conductive substrate. An electrodeposition solution composed of $HAuCl_{4(aq.)}$ (5 mM), $CTAC_{(aq.)}$ (10 mM) and $NaNO_{3(aq.)}$ (20 mM) were prepared in DI water. At a controlled temperature of 298 K, Au nanowires (NWs) were grown onto the flexible substrate (cathode) at 0.7 V by using a two-electrode electrochemical deposition system. A carbon electrode was used as the anode. After 24 h, the flexible electrode was isolated, rinsed with alcohol and DI water, and then dried with a flowing stream of $N_{2(g)}$.

Fabrication of nanosized MnO_2 spines on Au stems (NMSAS) on a flexible substrate

MnO_2 was coated on Au NWs *via* a two-electrode electrochemical deposition process. The as-prepared flexible substrate with deposited Au NWs was used as the anode while a carbon electrode was used as the cathode. An electrodeposition solution (pH 6) composed of $Mn(NO_3)_{2(aq.)}$ (20 mM) and $NaNO_{3(aq.)}$ (100 mM) was prepared. At 298 K, MnO_2 was electrochemically deposited at 1.5 V (0.85 V *vs.* Ag/AgCl) onto the Au NWs. After a designated time period (10, 15, 20, or 30 min), the flexible electrode was isolated, rinsed with alcohol and DI water, and then dried with a flowing stream of $N_{2(g)}$. The as-fabricated NMSAS electrode was stored for further investigations. To estimate the amounts of MnO_2 deposited on Au NWs, the electric currents applied were recorded. The data were converted into masses by Faraday's law (Table S1 in the ESI†).

Electrochemical capacitance analyses

Conventional three-electrode and two-electrode systems were employed for all electrochemical analyses. In the three-electrode system, the working electrode was a NMSAS electrode (1 cm × 1 cm) while the counter and reference ones were a Pt wire and an Ag/AgCl electrode, respectively. In the two-electrode system, two pieces of NMSAS were assembled face-to-face with a separator membrane. CV experiments were performed at various scan rates 2, 5, 10, 20, 30, 50, 80 and 100 mV s^{-1}. GV charge/discharge curves were obtained at various current densities 1, 2, 5, 10, 20, 30, 40, and 50 A g^{-1}. Current densities were estimated based on the total mass of MnO_2 on two electrodes in the two-electrode device tests. A potential window of 0–0.8 V was used in all the measurements. EIS data were recorded in the frequency range of 10^{-1} to 10^5 Hz with a mean voltage of 0 V and an amplitude of 5 mV. All electrochemical analyses were performed in $Na_2SO_{4(aq.)}$ (1 M) at room temperature.

Fabrication of the solid-state supercapacitor

A PVA–H_3PO_4 gel electrolyte was prepared by adding PVA powder (4 g) into $H_3PO_{4(aq.)}$ (1 M, 20 mL). The whole mixture was heated and stirred at 358 K until a clear solution was formed. Two NMSAS electrodes (2 cm × 1 cm) were immersed into the PVA–H_3PO_4 solution, removed, and assembled face-to-face with a separator membrane. After the gel solidified at room temperature, the solid-state supercapacitor device was obtained.

Results and discussion

To obtain NMSAS, a process involving two electrochemical deposition steps was carried out. Initially, high density Au nanowires (NWs) were electrochemically grown on a flexible PET substrate *via* a simple template-free procedure reported recently.[47,48] Then, thin layers of nanostructured MnO_2 (see below for characterizations) were covered uniformly onto the NW stems *via* another electrochemical deposition in a solution containing $Mn(NO_3)_{2(aq.)}$ and $NaNO_{3(aq.)}$ under a condition suggested by the corresponding Pourbaix diagram.[49,50] Detailed experimental steps and conditions are discussed in the Experimental section. In Fig. 1 and S1 and S2 in the ESI,† the results from SEM, TEM, and EDS investigations of bare Au NWs and NMSAS with a MnO_2 plating time of 10–30 min on flexible PET substrates are shown. The Au NWs (diameters 20–100 nm and lengths 10–20 μm) are dense and have a high-aspect ratio, as displayed in Fig. 1a. Nanosized stipule-like spines on stems are observed after MnO_2 was coated onto the NWs (Fig. 1b and c). The EDS studies (Fig. S2†) confirm that the samples contained Au, Mn and O atoms in the nanostructures. The atomic ratios of

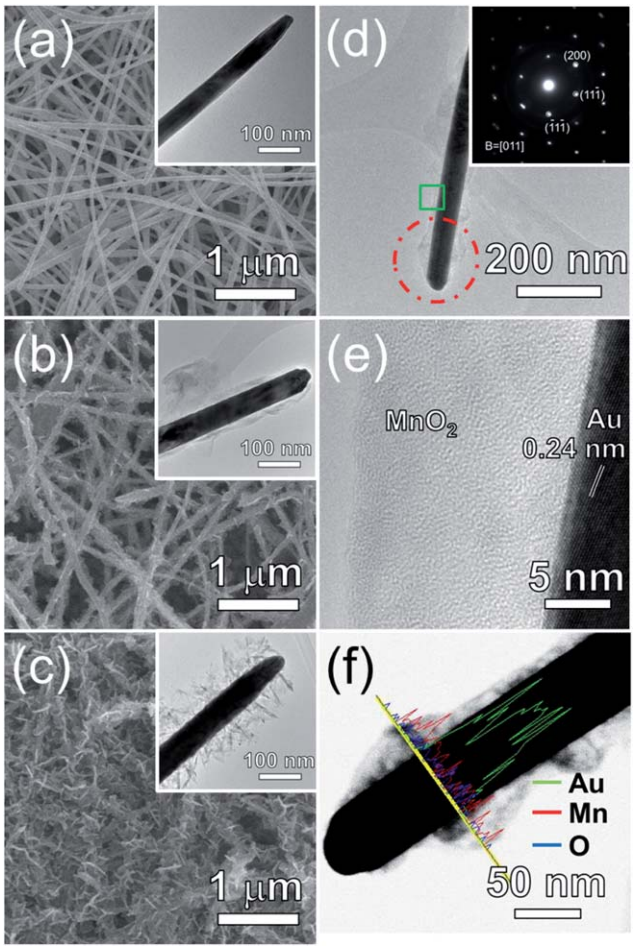

Fig. 1 Characterizations of nanostructures on flexible PET substrates. Low magnification SEM and TEM images (insets): (a) Au NWs, (b and c) NMSAS with a MnO_2 plating time of 15 min and 30 min, respectively. (d) TEM image and the SAED pattern (inset, from the red circle) of a NMSAS (MnO_2 plating time: 15 min). (e) Lattice-resolved HRTEM image from the green square in (d). (f) TEM image with line-scan EDS profiles (green: Au, red: Mn, and blue: O) of a NMSAS (MnO_2 plating time: 15 min).

Mn to O in the samples are approximately one to two. The TEM image of a typical NMSAS is displayed in Fig. 1d. As shown in the image, the one-dimensional (1D) nanomaterial has a spiny stem structure. The SAED pattern (inset, Fig. 1d) from the circled area can be indexed to a single crystal faced-centred cubic (FCC) Au NW with the [011] zone axis. No other diffraction patterns can be found, suggesting that the stipular spines outside the stem are amorphous. A high resolution TEM (HRTEM) image in Fig. 1e, enlarged from the rectangular area in Fig. 1d, confirms that the Au core is covered by an amorphous shell with a thickness of 15–20 nm. The fringe from the crystalline core has a spacing of 0.24 nm, which can be assigned to the [111] planes of Au. EDS line-scan profiles displayed in Fig. 1f reveal that the signal of Au is from the core while the ones of Mn and O are from the outer shell. The results from high resolution XPS studies are presented in Fig. S3 in the ESI.† In Fig. S3a,† two peaks centered at 642.3 and 653.8 eV are assigned to the binding energies of Mn $2p_{3/2}$ and Mn $2p_{1/2}$ electrons, respectively. Curve fittings of the signals provide multiple splittings due to electrostatic, spin-orbital, and crystal field interactions. This result is consistent with the XPS signals of MnO_2 reported previously.[51] The peaks at 529.7 and 531.2 eV (Fig. S3b†) are assigned to O 1s electrons in Mn–O–Mn and Mn–OH, respectively.[51] Finally, as displayed in Fig. S3c,† the peaks at 84.2 and 87.8 eV are assigned to Au $4f_{7/2}$ and Au $4f_{5/2}$ electrons in Au(0).[52] To estimate the amounts of MnO_2 deposited on NWs, applied deposition currents were recorded and converted into masses by Faraday's law (Table S1 in the ESI†). The masses increased linearly with the increasing plating time from 10 to 30 min (see Fig. 2b). In addition, the surface roughness and thickness of the spiny layers increased as well, as presented in the SEM and TEM images in Fig. S1.†

Electrochemical behaviors of Au NWs and NMSAS on flexible substrates were measured with a three-electrode system in $Na_2SO_{4(aq.)}$. Data from CV experiments are summarized in Fig. S4 in the ESI† and in Fig. 2. As shown in Fig. S4,† the Au NW electrode does not generate significant responses. This corresponds to the electrode's low charge storage capability. All NMSAS electrodes exhibit responses in approximately rectangular shapes. Their areas enlarged as the scan rates were increased from 2 to 100 mV s^{-1}. The observations reveal that NMSAS electrodes possess nearly ideal capacitive performances

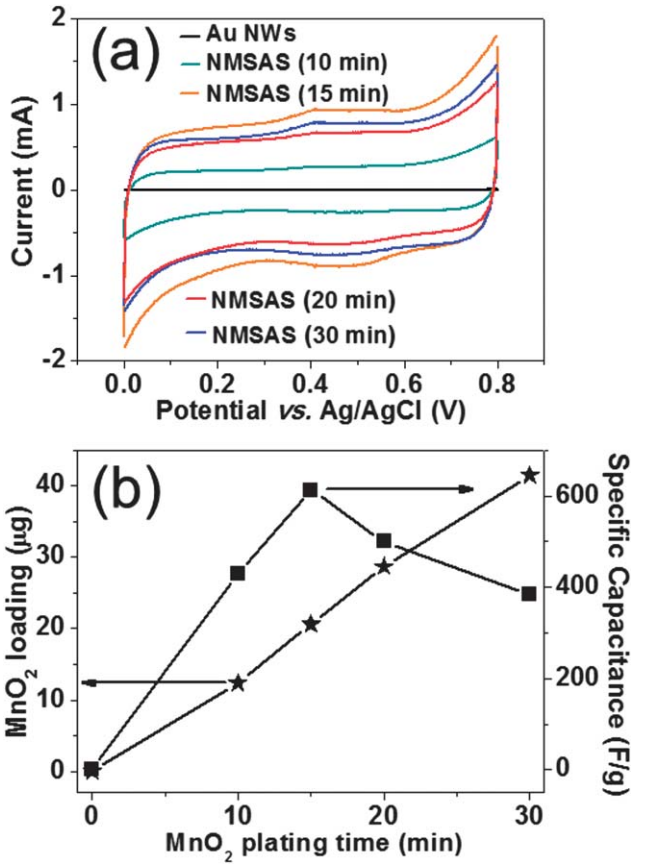

Fig. 2 (a) CV curves of Au NWs and NMSAS with different MnO_2 plating times (three-electrode system in $Na_2SO_{4(aq.)}$ (1 M) at 50 mV s^{-1}). (b) Plots of loaded MnO_2 masses (★) and specific capacitances (■) at 50 mV s^{-1} *versus* MnO_2 plating times.

and good high-rate capabilities. By ignoring the contribution from the Au NW stems, variations of specific capacitances to scan rates of the NMSAS electrodes are derived from their CV data and illustrated in Fig. S4f.† At a low scan rate of 2 mV s^{-1}, the NMSAS electrode with a MnO_2 plating time of 15 min reveals an excellent capacitance performance of 1130 F g^{-1}. Even at a high scan rate of 100 mV s^{-1}, the electrode provides an extremely high capacitance of 600 F g^{-1}. The CV data of the electrodes recorded at 50 mV s^{-1} are shown in Fig. 2. Fig. 2a confirms that the NMSAS electrode with a MnO_2 plating time of 15 min provides the best performance. In Fig. 2b, masses of MnO_2 loaded on the electrodes and the corresponding specific capacitances are plotted against the MnO_2 plating time. The specific capacitance maximized at the plating time of 15 min. Therefore, MnO_2 spines with an appropriate thickness are necessary for providing the supercapacitance performance. As displayed in Fig. 1b and d, the NMSAS has thin MnO_2 spines of 15–20 nm and open spaces among the nanostructures. In addition, highly conductive Au NW stems could maximize the charge transportation in and out of the spiny oxide shells. This electrode will be investigated further (see below) to demonstrate its potential for supercapacitor applications. On the other hand, after more MnO_2 is loaded, excessive spiny nanostructures, as presented in Fig. 1c, may seal interstices among the stems, and prevent effective electrode–electrolyte contact formation. Consequently, specific capacitances decreased after extended MnO_2 depositions.

Specific capacitances can be estimated by using three-electrode and two-electrode systems. In a three-electrode system, a reference electrode is needed in the cell to obtain the capacitance of the working electrode. On the other hand, a two-electrode system mimics a real supercapacitor device. According to the literature, the specific capacitance values measured from three-electrode (C_{3E}) and two-electrode (C_{2E}) techniques follow the equation $C_{3E} = 4 \times C_{2E}$.[53,54] CV data of the NMSAS electrode (MnO_2 deposition for 15 min) in $Na_2SO_{4(aq.)}$ (1 M) are shown in Fig. S5 in the ESI.† The result from the three-electrode system (Fig. S5a†) suggests that the specific capacitances decrease from 1010 to 600 F g^{-1} as the scan rates are increased from 2 to 100 mV s^{-1}. Using the CV data from a two-electrode system (Fig. S5b†), the specific capacitances are estimated to be 215 to 150 F g^{-1} as the scan rates are increased from 2 to 100 mV s^{-1}. The ratios of C_{3E} and C_{2E} in Fig. S5c† are close to 4. This agrees with the equation mentioned above.[53,54]

GV charge/discharge curves (Fig. 3a) of the best performed NMSAS electrode, with MnO_2 deposition for 15 min, are measured in $Na_2SO_{4(aq.)}$ employing a two-electrode system. Different current density charging/discharging cycles display quasi-symmetric triangles. Again, the data indicate that the electrode has an excellent electrochemical capacitive

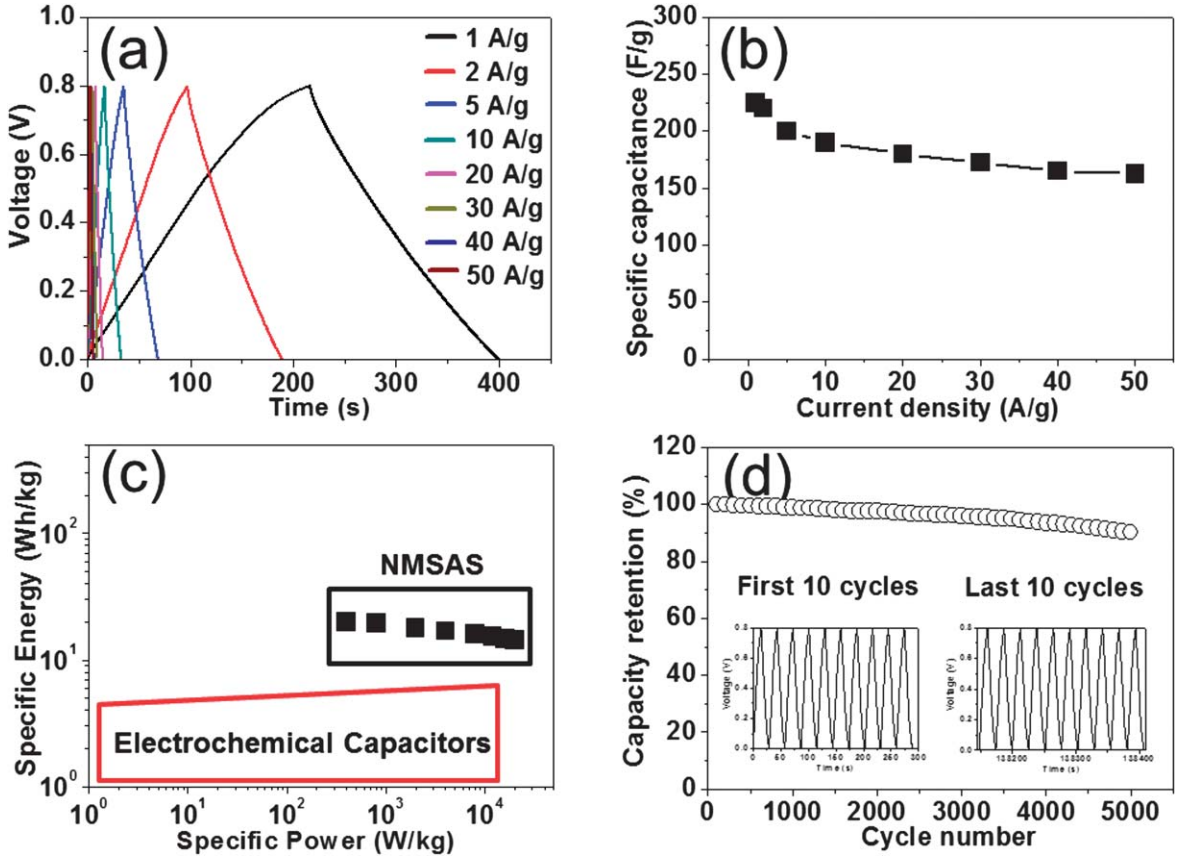

Fig. 3 GV constant-current charge/discharge studies of NMSAS (MnO_2 plating time, 15 min) on flexible PET substrates (two-electrode system, in $Na_2SO_{4(aq.)}$ (1 M)). (a) Constant current charge/discharge curves of different current densities (1–50 A g^{-1}). (b) Specific capacitances at various current densities. (c) Ragone plot of estimated specific energy and specific power at various charge/discharge rates. (d) Charge/discharge cycling tests at 10 A g^{-1} (inset: left, first ten cycles; right, last ten cycles).

character.[55] This corresponds well to the superior reversible redox behaviour observed in the CV tests (Fig. S4†). Specific capacitances calculated from the discharging curves (for details, see ESI†) at different charge/discharge rates (current densities) are plotted in Fig. 3b. The maximum specific capacitance of the hybrid material is calculated to be 225 F g^{-1} at 1 A g^{-1}. Even at a high charge/discharge rate of 50 A g^{-1}, the specific capacitance remains at a high value of 165 F g^{-1}. Specific energy and specific power are two important factors to be considered when electrochemical supercapacitors are developed for power applications.[2] A good electrochemical supercapacitor is expected to provide both high specific energy and specific capacitance at high charging/discharging rates. The Ragone plot (specific energy *versus* specific power) of the NMSAS electrode is illustrated in Fig. 3c. It is derived, as described in the ESI,† from the discharging curves measured at different charge/discharge rates. As the GV charge/discharge currents are increased from 1 to 50 A g^{-1}, the specific energy values decrease from 20 to 15 W h kg^{-1} while the specific power values increase from 0.4 to 20 kW kg^{-1}. These values are much higher than those of conventional electrochemical capacitors, as shown in the Ragone plot.[2] More importantly, the highest specific power value, 20 kW kg^{-1}, of the NMSAS electrode exceeds the target value of "Partnership for a New Generation of Vehicles" (PNGV), 15 kW kg^{-1}.[56,57] Another important requirement for supercapacitor applications is the long-term cycling stability. In Fig. 3d, the result from five thousand GV charge/discharge cycles of the NMSAS electrode at 10 A g^{-1} is shown. After the experiment was completed, only 10% of the specific capacitance was lost. Shapes of the last ten cycles remain nearly identical to the first ten cycles (see insets in Fig. 3d), revealing an excellent long-term cyclic performance.

All of the above results confirm that the NMSAS design maximizes the supercapacitor performance. This may be attributed to the following reasons. The first one is the large surface area provided by the spiny stem nanostructure. It offers efficient heterogeneous interactions between the electrolyte ions and the thin MnO_2 layers. The second one is due to the high electrical conductivity of Au NW stems. Although amorphous MnO_2 has an intrinsically low conductivity, which would restrict the charge/discharge rate, the spiny stem design could enhance the electrochemical capacitance by offering fast ion diffusions and efficient electron transportations. The last reason may be attributed to the amorphous nature of the spiny MnO_2 shells. This would enable fast and reversible redox reactions, which improve the specific capacitance and the long-term cycling stability.[41–46]

To examine whether NMSAS can be applied for flexible capacitors, a simple solid-state device, as shown in Fig. 4a, was

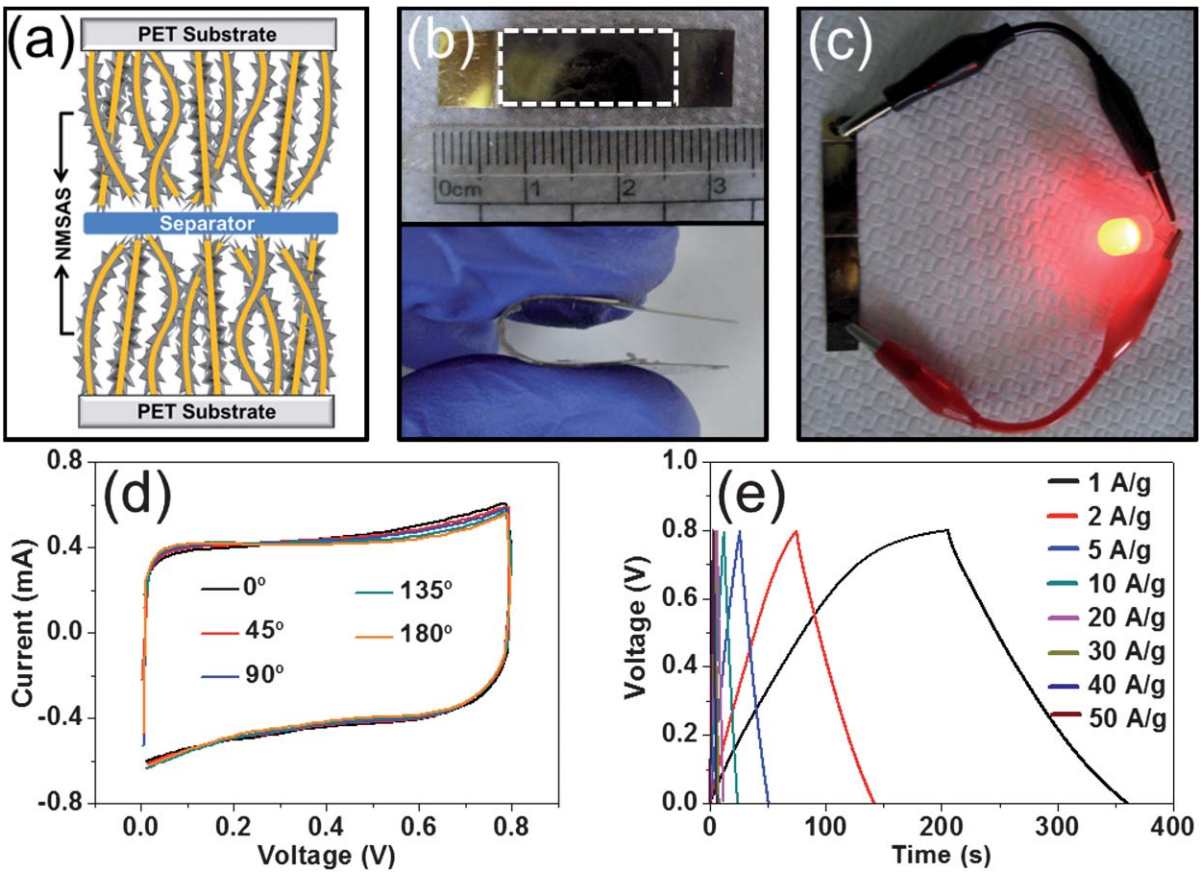

Fig. 4 (a) Schematic drawing of a solid-state NMSAS supercapacitor device (MnO_2 plating time: 15 min). (b) Optical photographs of the as-fabricated device. Top: white square indicates the capacitance region. Bottom: a highly bent device. (c) A LED powered by an assembly of two supercapacitors connected in series. (d) CV curves of a NMSAS supercapacitor with bending angles of 0°, 45°, 90°, 135°, and 180°. (e) GV charging/discharging curves of a NMSAS supercapacitor at various current densities.

Table 1 Comparison of supercapacitors

Electrode materials	Specific capacitance (F g^{-1})[a]	Specific power (kW kg^{-1})	Specific energy (W h kg^{-1})	Reference
Nanosized MnO_2 spines on Au stems (NMSAS)	165 (50 A g^{-1})	20	15	This study
Three-dimensional graphene/MnO_2 composite	50 (10 A g^{-1})[b]	5[b]	7	61
Multisegmented Au–MnO_2/carbon nanotube hybrid coaxial arrays	69 (6.6 A g^{-1})	2.3[b]	4.7	62
MnO_2/carbon fiber array	70 (15 A g^{-1})	6.2	6.2	63
Polyaniline–MnO_2 coaxial nanofiber	134 (20 A g^{-1})	10	18.6	64
Ultrafine MnO_2 nanowire	152 (20 A g^{-1})	10[b]	21.1[b]	65
Two-dimensional MnO_2/graphene hybrid nanostructures	208 (10 A g^{-1})	3.5[b]	14.2[b]	66

[a] Measured at different current densities by a GV charge/discharge test in Na_2SO_4(aq.) with a two-electrode system. [b] Estimated from the reference data.

fabricated by joining two NMSAS electrodes immersed in polyvinyl alcohol (PVA)–H_3PO_4 gel with a piece of central separator. The PVA–H_3PO_4 gel is a proton conducting polymeric solid-state electrolyte. H_3PO_4 provides H^+ ions, which would enhance the conductivity.[58,59] The as-fabricated solid-state device is not only lightweight but also highly flexible. It can be bent freely between 0–180°, as shown in Fig. 4b (see Fig. S6 in the ESI† for the bending angle definition). After the two devices were connected in series using Cu tape and charged at 1.5 V, the assembly powered a light-emitting diode (LED), as displayed in Fig. 4c. CV scans of the device at different degrees of bending are presented in Fig. 4d. They demonstrate that the electrochemical performance of the as-fabricated solid-state supercapacitor does not change much. In addition, the rectangular shapes of the symmetrical CV scans reveal that the device performed fast redox reactions in the PVA–H_3PO_4 solid electrolyte in a nearly ideal manner. The constant-current GV charge/discharge curves of the as-fabricated solid-state supercapacitor show quasi-symmetric triangles at several different current densities of 1–50 A g^{-1} in Fig. 4e. The observation indicates again that the supercapacitor provides good electrochemical performance. The maximum specific capacitance of the as-fabricated solid-state supercapacitor is calculated to be 195 F g^{-1} at 1 A g^{-1}. Even at a high charge/discharge rate of 50 A g^{-1}, the specific capacitance remains at a respectable value of 135 F g^{-1}. The as-fabricated solid-state supercapacitor was further investigated by electrochemical impedance spectroscopy (EIS) in the frequency range of 10^{-1} to 10^5 Hz. As shown in the Nyquist plot in Fig. S7 in the ESI,† a steep straight line close to the imaginary axis is observed. This suggests that the capacitive performance of the device is nearly ideal.[60] The real axis intercept is found at *ca.* 2 Ω. This manifests that both the electrodes and the electrolyte are highly conductive. All of the above results reveal the potential of the NMSAS electrode for flexible supercapacitor energy storage device applications.

Conclusion

In summary, we demonstrate a facile process to fabricate NMSAS on flexible PET substrates for supercapacitor electrodes. The high density hybrid nanomaterials were grown by two simple electrochemical deposition steps. These involved the deposition of Au NW stems on the substrates followed by plating spiny amorphous MnO_2 shells onto their surfaces. The maximum specific capacitance is measured to be 1130 F g^{-1} by CV (scan rate 2 mV s^{-1}) with the three-electrode configuration. From the GV charge/discharge tests using the two-electrode system, a maximum capacitance of 225 F g^{-1} (current density 1 A g^{-1}) is obtained. Even at a high charge/discharge rate of 50 A g^{-1}, the specific capacitance remains at a high value of 165 F g^{-1}. The electrode also exhibited excellent rate capability. Both the specific energy and the specific power values at 50 A g^{-1} are high, 15 W h kg^{-1} and 20 kW kg^{-1}, respectively. Its long-term cycling stability at 10 A g^{-1} is also excellent. After five thousand cycles, it loses only 10% of the initial specific capacitance. In comparison with other MnO_2 containing supercapacitor materials discussed in recent reports, as summarized in Table 1, our NMSAS performed outstandingly.[61–66] In addition, a pair of NMSAS electrodes were fabricated into a simple highly flexible solid-state device showing superior supercapacitance performance. All these results suggest that the hybrid material containing nanosized MnO_2 spines on metal stems are promising for the next generation high-performance supercapacitor applications.

Acknowledgements

We are grateful to the support from the National Science Council, "Aim for the Top University Plan" of the National Chiao Tung University, and the Ministry of Education of Taiwan, the Republic of China.

Notes and references

1 J. R. Miller and P. Simon, *Science*, 2008, **321**, 651.
2 P. Simon and Y. Gogotsi, *Nat. Mater.*, 2008, **7**, 845.
3 H. Nishide and K. Oyaizu, *Science*, 2008, **319**, 737.
4 M. Armand and J. M. Tarascon, *Nature*, 2008, **451**, 652.
5 G. Wang, L. Zhang and J. Zhang, *Chem. Soc. Rev.*, 2012, **41**, 797.
6 M. Kaempgen, C. K. Chan, J. Ma, Y. Cui and G. Gruner, *Nano Lett.*, 2009, **9**, 1872.

7 L.-L. Zhang and X.-S. Zhao, *Chem. Soc. Rev.*, 2009, **38**, 2520.
8 M. F. El-Kady, V. Strong, S. Dubin and R. B. Kaner, *Science*, 2012, **335**, 1326.
9 C.-C. Hu, K.-H. Chang, M.-C. Lin and Y.-T. Wu, *Nano Lett.*, 2006, **6**, 2690.
10 E. Seo, T. Lee, K.-T. Lee, H.-K. Song and B.-S. Kim, *J. Mater. Chem.*, 2012, **22**, 11598.
11 X. Lu, D. Zheng, T. Zhai, Z. Liu, Y. Huang, S. Xie and Y. Tong, *Energy Environ. Sci.*, 2011, **4**, 2915.
12 A. J. Roberts and R. C. T. Slade, *J. Mater. Chem.*, 2010, **20**, 3221.
13 X.-H. Xia, J.-P. Tu, Y.-J. Mai, X.-L. Wang, C.-D. Gu and X.-B. Zhao, *J. Mater. Chem.*, 2011, **21**, 9319.
14 C. Yuan, L. Yang, L. Hou, L. Shen, F. Zhang, D. Li and X. Zhang, *J. Mater. Chem.*, 2011, **21**, 18183.
15 K. Liang, X. Tang and W. Hu, *J. Mater. Chem.*, 2012, **22**, 11062.
16 B. Wang, J. S. Chen, Z. Wang, S. Madhavi and X. W. Lou, *Adv. Energy Mater.*, 2012, **2**, 1188.
17 S. Boukhalfa, K. Evanoff and G. Yushin, *Energy Environ. Sci.*, 2012, **5**, 6872.
18 B. Saravanakumar, K. K. Purushothaman and G. Muralidharan, *ACS Appl. Mater. Interfaces*, 2012, **4**, 4484.
19 X. Lu, G. Wang, T. Zhai, M. Yu, J. Gan, Y. Tong and Y. Li, *Nano Lett.*, 2012, **12**, 1690.
20 C. Xiang, M. Li, M. Zhi, A. Manivannan and N. Wu, *J. Mater. Chem.*, 2012, **22**, 19161.
21 Y.-G. Wang, H.-Q. Li and Y.-Y. Xia, *Adv. Mater.*, 2006, **18**, 2619.
22 S. Biswas and L. T. Drzal, *Chem. Mater.*, 2010, **22**, 5667.
23 G. A. Snook, P. Kao and A. S. Best, *J. Power Sources*, 2011, **196**, 1.
24 J. Jiang, Y. Li, J. Liu, X. Huang, C. Yuan and X.-W. Lou, *Adv. Mater.*, 2012, **24**, 5166.
25 C. D. Lokhande, D. P. Dubal and O.-S. Joo, *Curr. Appl. Phys.*, 2011, **11**, 255.
26 W. Wei, X. Cui, W. Chen and D. G. Ivey, *Chem. Soc. Rev.*, 2011, **40**, 1697.
27 R. N. De Guzman, A. Awaluddin, Y.-F. Shen, Z. R. Tian, S. L. Suib, S. Ching and C.-L. O'Young, *Chem. Mater.*, 1995, **7**, 1286.
28 R. Jiang, T. Huang, J. Liu, J. Zhuang and A. Yu, *Electrochim. Acta*, 2009, **54**, 3047.
29 T. Xue, C.-L. Xu, D.-D. Zhao, X.-H. Li and H.-L. Li, *J. Power Sources*, 2007, **164**, 953.
30 X. Lang, A. Hirata, T. Fujita and M. Chen, *Nat. Nanotechnol.*, 2011, **6**, 232.
31 Q. Li, Z.-L. Wang, G.-R. Li, R. Guo, L.-X. Ding and Y.-X. Tong, *Nano Lett.*, 2012, **12**, 3803.
32 G. Yu, L. Hu, M. Vosgueritchian, H. Wang, X. Xie, J. R. McDonough, X. Cui, Y. Cui and Z. Bao, *Nano Lett.*, 2011, **11**, 2905.
33 L. Hu, W. Chen, X. Xie, N. Liu, Y. Yang, H. Wu, Y. Yao, M. Pasta, H. N. Alshareef and Y. Cui, *ACS Nano*, 2011, **5**, 8904.
34 Z. Fan, J. Yan, T. Wei, L. Zhi, G. Ning, T. Li and F. Wei, *Adv. Funct. Mater.*, 2011, **21**, 2366.
35 A. L. M. Reddy, M. M. Shaijumon, S. R. Gowda and P. M. Ajayan, *J. Phys. Chem. C*, 2009, **114**, 658.
36 Y. Cheng, S. Lu, H. Zhang, C. V. Varanasi and J. Liu, *Nano Lett.*, 2012, **12**, 4206.
37 W. Chen, R. B. Rakhi, L. Hu, X. Xie, Y. Cui and H. N. Alshareef, *Nano Lett.*, 2011, **11**, 5165.
38 R. Liu and S.-B. Lee, *J. Am. Chem. Soc.*, 2008, **130**, 2942.
39 R. Liu, J. Duay and S.-B. Lee, *ACS Nano*, 2010, **4**, 4299.
40 J. Han, L. Li, P. Fang and R. Guo, *J. Phys. Chem. C*, 2012, **116**, 15900.
41 X. Lu, T. Zhai, X. Zhang, Y. Shen, L. Yuan, B. Hu, L. Gong, J. Chen, Y. Gao, J. Zhou, Y. Tong and Z.-L. Wang, *Adv. Mater.*, 2012, **24**, 938.
42 J. Yan, E. Khoo, A. Sumboja and P. S. Lee, *ACS Nano*, 2010, **4**, 4247.
43 J. Duay, E. Gillette, R. Liu and S. B. Lee, *Phys. Chem. Chem. Phys.*, 2012, **14**, 3329.
44 X. Lu, M. Yu, G. Wang, T. Zhai, S. Xie, Y. Ling, Y. Tong and Y. Li, *Adv. Mater.*, 2013, **25**, 267.
45 L. Bao, J. Zang and X. Li, *Nano Lett.*, 2011, **11**, 1215.
46 W. Yan, J. Y. Kim, W. Xing, K. C. Donavan, T. Ayvazian and R. M. Penner, *Chem. Mater.*, 2012, **24**, 2382.
47 Y.-L. Chen, C.-Y. Lee and H.-T. Chiu, *J. Mater. Chem. B*, 2013, **1**, 186.
48 M.-S. Hsu, Y.-L. Chen, C.-Y. Lee and H.-T. Chiu, *ACS Appl. Mater. Interfaces*, 2012, **4**, 5570.
49 M. Pourbaix, *Atlas d'Equilibres Electrochimiques*, Gauthier-Villars, Paris, 1963.
50 D. Portehault, S. Cassaignon, E. Baudrin and J.-P. Jolivet, *J. Mater. Chem.*, 2009, **19**, 2407.
51 H. W. Nesbitt and D. Banerjee, *Am. Mineral.*, 1998, **83**, 305.
52 J. F. Moulder, W. E. Stickle, P. E. Sobol and K. D. Bomben, *Handbook of X-ray Photoelectron Spectroscopy*, Perkin-Elmer Corp., Eden Prairie, MN, 1995.
53 D. Qu and H. Shi, *J. Power Sources*, 1998, **74**, 99.
54 M. D. Stoller and R. S. Ruoff, *Energy Environ. Sci.*, 2010, **3**, 1294.
55 J. P. Zheng and T. R. Jow, *J. Power Sources*, 1996, **62**, 155.
56 B. Scrosati, *Nature*, 1995, **373**, 557.
57 D.-W. Wang, F. Li, M. Liu, G.-Q. Lu and H.-M. Cheng, *Angew. Chem.*, 2008, **120**, 379.
58 P. N. Gupta and K. P. Singh, *Solid State Ionics*, 1996, **86–88**(part 1), 319.
59 S. A. Hashmi, R. J. Latham, R. G. Linford and W. S. Schlindwein, *Polym. Int.*, 1998, **47**, 28.
60 R. Kötz and M. Carlen, *Electrochim. Acta*, 2000, **45**, 2483.
61 Y. He, W. Chen, X. Li, Z. Zhang, J. Fu, C. Zhao and E. Xie, *ACS Nano*, 2012, **7**, 174.
62 A. L. M. Reddy, M. M. Shaijumon, S. R. Gowda and P. M. Ajayan, *J. Phys. Chem. C*, 2009, **114**, 658.
63 J. Liu, J. Essner and J. Li, *Chem. Mater.*, 2010, **22**, 5022.
64 H. Jiang, J. Ma and C. Li, *J. Mater. Chem.*, 2012, **22**, 16939.
65 H. Jiang, T. Zhao, J. Ma, C. Yan and C. Li, *Chem. Commun.*, 2011, **47**, 1264.
66 L. Peng, X. Peng, B. Liu, C. Wu, Y. Xie and G. Yu, *Nano Lett.*, 2013, **13**, 2151.